Cross-Gradient Joint Inversion of DC Resistivity and Gravity Gradient Data: A Multi-Disciplinary Approach for Geoscience, Heritage, and the Built Environment.

remote sensing

MDPI

Article

Cross-Gradient Joint Inversion of DC Resistivity and Gravity Gradient Data: A Multi-Disciplinary Approach for Geoscience, Heritage, and the Built Environment

Hosseinali Ghari [1], Saeed Parnow [2,3,*], Ramin Varfinezhad [4], Maurizio Milano [5], Francois Daniel Fourie [6] and Fabio Tosti [2,3]

[1] Department of Mining and Metallurgical Engineering, Yazd University, Yazd 8915818411, Iran; hghari@yazd.ac.ir
[2] School of Computing and Engineering, University of West London, London W5 5RF, UK; fabio.tosti@uwl.ac.uk
[3] The Faringdon Research Centre for Non-Destructive Testing and Remote Sensing, University of West London, London W5 5RF, UK
[4] Department of Earth Physics, Institute of Geophysics, University of Tehran, Tehran 1435944411, Iran; ramin.varfi@ut.ac.ir
[5] Department of Earth, Environmental and Resources Science, University of Naples Federico II, 80126 Naples, Italy; maurizio.milano@unina.it
[6] Institute for Groundwater Studies, University of the Free State, Bloemfontein 9300, South Africa; fouriefd@ufs.ac.za
* Correspondence: saeed.parnow@student.uwl.ac.uk

Abstract: Accurate subsurface imaging is crucial for understanding complex geological structures. Traditional approaches often involve separate inversion of different geophysical datasets, which may not fully capture the structural similarities between the models. Joint inversion, integrating multiple datasets, offers a more comprehensive view by enhancing the resolution and the accuracy of subsurface models. In this study, we propose a joint inversion technique for DC resistivity and vertical gravity gradient data, leveraging the cross-gradient constraint to enforce structural similarities between the resulting models. This method is applied to both synthetic and real datasets, including case studies involving qanats in Iran and a dolerite dyke in South Africa. The results demonstrate that joint inversion significantly improves the accuracy of resistivity and density models compared to independent inversion, particularly in resolving intricate geological features. This approach has proven effective in enhancing subsurface mapping for multi-disciplinary purposes, including resource exploration, heritage conservation, and risk mitigation for the built environment.

Keywords: cross-gradient joint inversion; DC resistivity; vertical gravity gradient; dolerite dyke; qanats; resource exploration; heritage conservation; built environment

Citation: Ghari, H.; Parnow, S.; Varfinezhad, R.; Milano, M.; Fourie, F.D.; Tosti, F. Cross-Gradient Joint Inversion of DC Resistivity and Gravity Gradient Data: A Multi-Disciplinary Approach for Geoscience, Heritage, and the Built Environment. *Remote Sens.* **2024**, *16*, 4468. https://doi.org/10.3390/rs16234468

Academic Editors: Daniele Cirillo, Francesco Brozzetti and Pietro Tizzani

Received: 31 October 2024
Revised: 24 November 2024
Accepted: 24 November 2024
Published: 28 November 2024

1. Introduction

The ambiguity and uncertainty associated with the separate inversion of different geophysical datasets can be mitigated through appropriate integration, depending on the specific conditions. To this purpose, several methods have been developed, each tailored to specific applications and data types. For example, local, global, and combined optimisation methods have been developed to link models from different datasets [1,2]. Petrophysical joint inversion links the models of different datasets through a shared petrophysical relationship, such as linking density and seismic velocity [3]. Another approach is the joint inversion based on fuzzy clustering, where the subsurface is divided into clusters with similar physical properties across datasets [4]. A widely used method for integrating geophysical data is the cross-gradient joint inversion, which relies on the assumption of structural similarities between the inverse models derived from the different datasets. Ever

since Gallardo et al. [5] successfully developed this approach for joint inversion of DC resistivity and seismic data, the cross-gradient joint inversion has been extensively used for the joint processing and interpretation of geophysical datasets.

The significance of this approach becomes apparent when conducting a search for the terms "cross-gradient" and "joint inversion" in the Scopus search engine, using the recommended method of searching within titles, abstracts, and keywords, as advised by [6]. Following a comprehensive screening of the titles, abstracts, and whole texts of the publications extracted from Scopus, a total of 129 journal papers and 53 conference articles in the English language were identified. These publications appeared between 2003 and 2023 and underscore the significance of the cross-gradient-based joint inversion technique. Despite fluctuations in the number of papers and articles appearing each year (Figure 1a), the use of this technique to integrate diverse geophysical datasets has shown a consistent upward trend, thus substantiating growing research attention towards this approach.

Furthermore, the VOSviewer software (1.6.20) was used to perform a bibliometric analysis and determine which geophysical datasets are most incorporated in joint inversion based on the cross-gradient approach. This analysis aimed to provide insights into the current research in this field and to provide a framework for organising the various geophysical techniques that have been used in studies on cross-gradient joint inversion.

Figure 1b is a cluster diagram showing the results of a bibliometric study that utilises the co-occurrence of important phrases (keywords, titles, and abstracts) in publications to establish connections between them. The VOSviewer software produced three discrete clusters of important phrases, each representing a grouping of geophysical methods in the cluster diagram, as summarised in Table 1. The observed clusters indicate the prevalence of papers involving the joint inversion of the following geophysical datasets: magnetic and gravity, electrical resistivity and seismic, seismic and electromagnetic, and Ground Penetrating Radar (GPR) and refraction seismic.

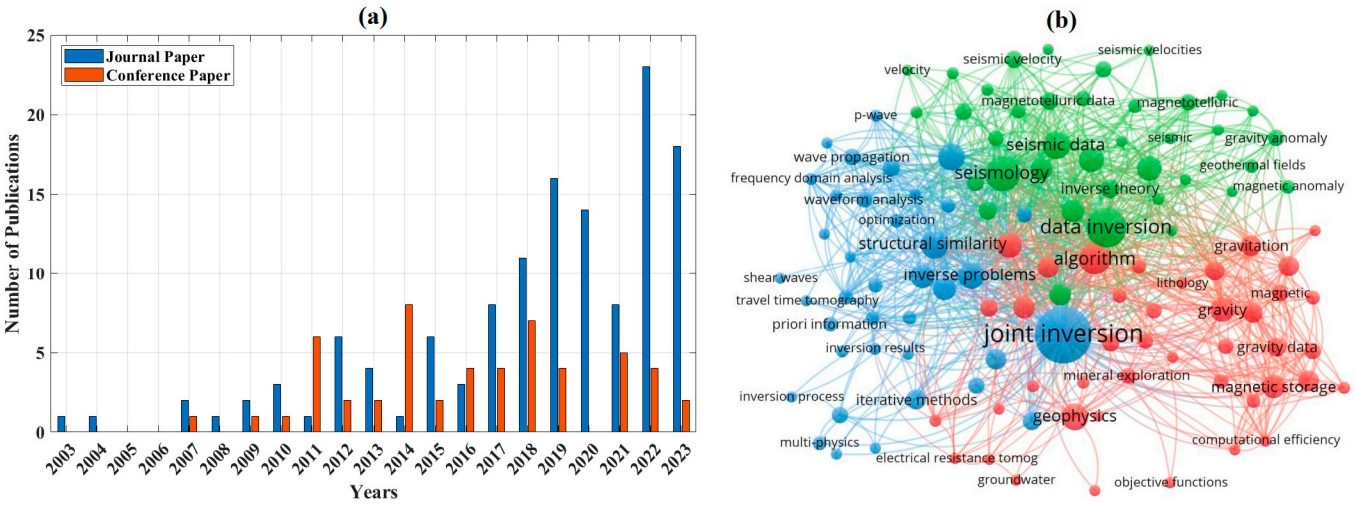

Figure 1. (**a**) Number of publications using cross-gradient joint inversion and (**b**) VOSviewer output of the co-occurrence of the keywords listed in Table 1 and terms relevant to cross-gradient joint inversion.

Table 1. Clusters of co-occurrences of different geophysical keywords and "cross-gradient joint inversion" as shown in Figure 1b.

Cluster	Colour	Label
1	Red	Gravity and Magnetic
2	Green	Magneto Telluric, Seismic (Reflection), Gravity, and Magnetic
3	Blue	EMFD, GPR, ERT, and Seismic (Refraction)

In particular, Gallardo et al. [7] used the cross-gradient constraint for the joint inversion of magnetotelluric (MT) and seismic data. They showed the effectiveness of the joint inversion algorithm for identifying deep structures and near-surface anomalies using synthetic and field datasets, respectively. Fregoso et al. [8] extended the cross-gradient function for joint inversion of magnetometric and gravity data. In addition, unlike [5,9], solving the joint inversion problem using Lagrangian multipliers, they utilised the generalised least-square formulation introduced by [10]. Cross-gradient-based joint inversion of frequency domain electromagnetic (FDEM) and seismic data was proposed by Hu et al. [11]. They applied the joint algorithm on three different synthetic cases, of which one was based on the real case of the gas reservoir in the Troll field in Norway. Furthermore, the regularisation parameter was chosen by an automatic procedure called the multiplicative regularisation technique, leading to the robustness of their algorithm without having any a priori information on the noise level.

Doetsch et al. [12] employed the cross-gradient constraint for joint inversion of time-lapse cross-hole electrical resistivity tomography (ERT) and GPR travel-time data. A normalised cross-gradient constraint was presented by Bennington et al. [13] for the joint inversion of seismic and magnetotelluric data. The normalised cross-gradient solved the cross-gradient problem related to having larger weights for cross-gradient values in the near surface relative to the deep parts. Joulidehsar et al. [14] introduced the compacting and depth weighting functions in the joint inversion algorithm of Fregoso et al. [8] and utilised the least squares QR factorisation (LSQR) technique to reduce the required computation time. Varfinezhad et al. [15] applied the algorithm for the joint inversion of DC resistivity and magnetic data by including a model weighting matrix derived from the multiplication of compactness and depth weighting constraints. Recently, Bianco et al. [16] proposed the multi-order sequential joint inversion of gravity data based on the cross-gradient constraint and inhomogeneous depth weighting. Other publications that have utilised the cross-gradient function for joint inversion include [17–21].

In this paper, our aim is to explore the joint inversion of DC resistivity and vertical gravity gradient (g_{zz}) data using cross-gradient, depth weighting, and compactness constraints, which, to our knowledge, have never been proposed before. The effectiveness of the algorithm will be shown by applying it to both synthetic and real field datasets.

In addition to filling the methodological gap in geophysical data processing, the proposed joint inversion technique offers significant practical applications. Qanats and dykes, essential for resource exploitation, historical preservation, and built environment risk mitigation, may significantly benefit from this methodology. Qanats, historical subterranean water networks found in areas such as Iran, are essential for comprehending subsurface water routes and alleviating the hazards of collapse that endanger contemporary infrastructure. Likewise, dykes, especially in areas such as South Africa, are essential for groundwater investigation and the comprehension of underlying formations. Individual geophysical data inversion methods struggle to characterise these features; however, resistivity and gravity gradient data inversion improve subsurface characterisation. This geophysical inversion approach has far-reaching implications for safer urban planning, resource management, and the preservation of culturally significant buildings.

2. Materials and Methods

We first derived equations describing the joint inversion of resistivity and vertical gravity gradient data using the cross-gradient constraint. Next, we developed an algorithm to apply these equations to synthetic and real datasets. Synthetic 2D apparent resistivity data were generated using the Res2DMod software (K3-FAF3A051-058E), whereas the gravity gradient forward response was calculated using the formula provided in Blakely [22]. Two synthetic models were considered. The first model domain has horizontal (x) and vertical (z) dimensions of 150 m and 50 m, respectively, and was divided into square prisms with side lengths of 2.5 m, resulting in 60 prisms in the x-direction and 20 in the z-direction (Figure 2). This model consists of three bodies, each with a resistivity of 20 Ωm and a

density contrast of 0.5 g/cm^3 with the background. These bodies have different sizes in the vertical and horizontal directions and are set at different depths (Figure 3). The resistivity of the homogeneous background was set at 100 Ωm. The complexity of this model was deemed sufficient for assessing the performance of the joint inversion technique [23,24].

The synthetic apparent resistivity data were calculated for the Wenner alpha configuration with unit electrode spacings ranging from 5 m to 40 m, for a total of 220 data points. For the vertical gravity gradient data (g_{zz}), 60 data points were modelled along the length of the profile at a spacing of 2.5 m.

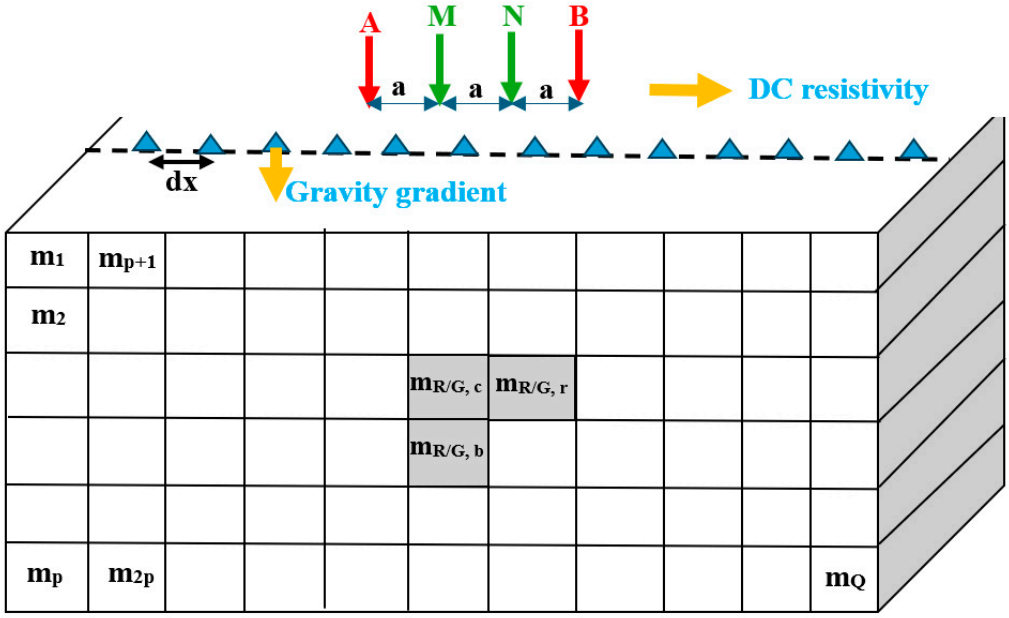

Figure 2. Model domain for the generation of synthetic 2D resistivity and vertical gravity gradient data. The three-cell framework, illustrated in grey, represents the discrete form of cross-gradients at any specific cell location within the model.

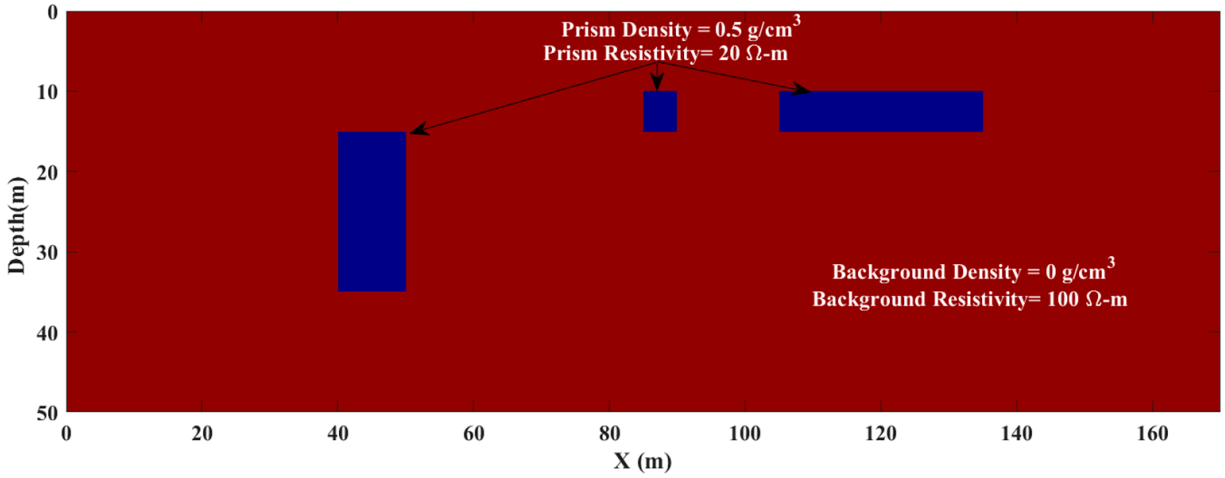

Figure 3. Model parameters of synthetic Model I.

The second synthetic test consists of a model domain of 295 m horizontal length and 40 m thickness. Here, we consider a thin vertical dyke with the top at a 5 m depth and the bottom at 10 m below the surface, located in the deeper layer of a two-layered medium (Figure 4a). The resistivity values of the first and second layers were set at 300 Ωm and 1000 Ωm (Figure 4a), respectively, whereas the vertical dyke has a resistivity of 50 Ωm and a density contrast of 0.5 g/cm^3 with respect to the background density (Figure 4b). The model

was divided into 59 cells in the horizontal direction and 16 cells in the vertical direction, consisting of rectangular prisms of size 5 × 2.5 m^2. The synthetic apparent resistivity data were computed using the Wenner alpha configuration, with electrode spacings ranging from 5 m to 40 m, producing 792 data points in total. For the vertical gravity gradient data (g_{zz}), 59 points were modelled along the profile, with measurements taken at 5 m intervals between stations.

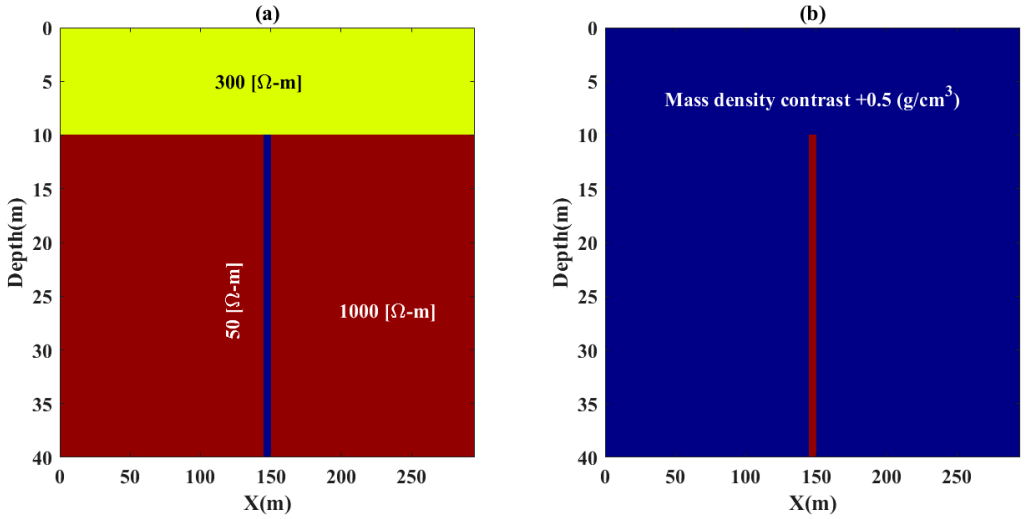

Figure 4. Model parameters of synthetic Model II. (**a**) Resistivity model representing a thin vertical dyke, and (**b**) the corresponding mass density model.

3. Theoretical Background

3.1. Forward Problem of Resistivity

Integral equations (IE), finite differences (FD), and finite elements (FE) are the most common techniques for DC resistivity modelling. For models composed of homogenous and layered backgrounds, the IE technique is faster than the FD and FE methods and it may produce a forward response as accurate as the FD and FE approaches [25]. In resistivity explorations, we are usually confronted with models including layered backgrounds [26]. Maxwell's equations exhibit nonlinearity in relation to the electrical resistivity (conductivity) parameter, making DC resistivity modelling a nonlinear problem according to Varfinezhad et al. [15]. In the current study, we use a linear IE approach developed by Pérez-Flores et al. [27] to conduct the forward resistivity modelling.

The Born approximation can be used to relate the apparent resistivity ρ_a to the true resistivity ρ in DC resistivity measurements as follows:

$$\log \rho_a(x_A, x_{B,} x_M, x_N) = \frac{[g]^{-1}}{\pi} \int_0^{\infty} \int_{-\infty}^{\infty} K(x_A, x_{B,} x_M, x_N, x, z) \log \rho(x, z) dx dz, \quad (1)$$

where x_A, x_B, x_M, and x_N represent the coordinates of the electrodes A, B, M, and N, respectively. The geometrical factor is denoted as g, and the kernel K consists of the following four terms:

$$\begin{aligned} K(x_A, x_{B,} x_M, x_N, x, z) \\ = N(x_A, x_M, x, z) - N(x_B, x_M, x, z) \\ -N(x_A, x_N, x, z) - N(x_B, x_N, x, z) \end{aligned} \quad (2)$$

where each term can be computed as follows [28]:

$$N(x_i, x_j, x, z) = \int_{-\infty}^{\infty} \frac{(x-x_i)(x_j-x)-y^2-z^2}{\sqrt{\left((x-x_i)^2+y^2+z^2\right)^3\left((x_j-x)^2+y^2+z^2\right)^3}} dy, \quad \begin{cases} i = A, B \\ j = M, N \end{cases} \tag{3}$$

To derive the 2D scenario, we assume P data points and split the source volume into Q prisms with infinite length in the y-direction and constant resistivity (Figure 2). The forward problem is thus expressed as follows:

$$\mathbf{d}_{\mathrm{R}} = \mathbf{A}_{\mathrm{R}}\mathbf{m}_{\mathrm{R}} \tag{4}$$

where the vector $\mathbf{d}_{\mathrm{R}}$ contains the logarithmically transformed data of ρ_a. The vector $\mathbf{m}_{\mathrm{R}}$ consists of unknown elements of $\log(\rho)$, and $\mathbf{A}_{\mathrm{R}}$ is a forward operator that can be calculated by discretising the following equation:

$$\mathbf{A}_{\mathrm{R}} = \frac{[g]^{-1}}{\pi} \int_0^{\infty} \int_{-\infty}^{\infty} K(x_A, x_B, x_M, x_N, x, z) dx dz \tag{5}$$

3.2. Forward Problem of the Gravity Gradient

Changes in the gravity field along the three axes result in the gravity gradient tensor. The most widely used component is the vertical gravity gradient (g_{zz}), which gives the rate of change of the vertical component of gravity at a certain height z. g_{zz} can be calculated by subtracting the gravity values at two places that are a minor vertical distance h apart, as follows:

$$g_{zz} = \frac{\partial g_z}{\partial z} \approx \frac{g_z(z + h/2) - g_z(z - h/2)}{h} \tag{6}$$

The forward gravity problem is expressed as a linear Fredholm integral equation of the first type, specifically for the g_{zz} component, represented in matrix form as follows [29]:

$$\mathbf{d}_{\mathrm{G}} = \mathbf{A}_{\mathrm{G}}\mathbf{m}_{\mathrm{G}} \tag{7}$$

where $\mathbf{d_G}$ is the data vector containing observed gravity gradient values, with a sample interval of dx as shown in Figure 2. $\mathbf{A_G}$ is the forward operator and $\mathbf{m_G}$ is the density model.

3.3. Cross-Gradient Joint Inversion Algorithm

Joint inversion of DC resistivity and gravity gradient data can be performed by using the approach proposed by Gallardo et al. [9]. The gradient of the model parameters, such as resistivity and density, is a beneficial function to use during the inversion because it accounts for variations in the physical properties of the subsurface in terms of both position and direction. In a 2D scenario, the cross-gradient function is defined as follows:

$$t = \nabla m_R(x, z) \times \nabla m_G(x, z) \tag{8}$$

The terms $m_R(x, z)$ and $m_G(x, z)$ represent the resistivity and density models, respectively. Expanding the variable t results in the following equation:

$$t(x, z) = \left(\frac{\partial m_{\mathrm{R}}(x, z)}{\partial z}\right)\left(\frac{\partial m_{\mathrm{G}}(x, z)}{\partial \mathrm{x}}\right) - \left(\frac{\partial m_{\mathrm{R}}(x, z)}{\partial x}\right)\left(\frac{\partial m_{\mathrm{G}}(x, z)}{\partial z}\right) \tag{9}$$

If the cross-gradient function has a zero value, it indicates that the two models are exactly similar from a structural perspective. In other words, both models display the same spatial variations. Following [9], Equation (9) can be simplified to the following:

$$t \cong \frac{4}{\Delta x \Delta z}[m_{Rc}(m_{Gb} - m_{Gr}) + m_{Rr}(m_{Gc} - m_{Gb}) + m_{Rb}(m_{Gr} - m_{Gc})] \tag{10}$$

In Equation (10), for a given cell (specified by subscript *c*), the next cells below and to the right of the cell are indicated by the subscripts *b* and *r*, respectively (Figure 2).

The objective function to be minimized under the cross-gradient constraint is defined as per [5], as follows:

$$min \left\{ \varphi(\mathbf{m}_R, \mathbf{m}_G) = \left\| \begin{matrix} \mathbf{d}_R - \mathbf{A}_R\mathbf{m}_R \\ \mathbf{d}_G - \mathbf{A}_G\mathbf{m}_G \end{matrix} \right\|^2_{\mathbf{C}_{\mathbf{dd}}^{-1}} + \left\| \begin{matrix} \alpha_R\mathbf{W}_{mR}\mathbf{m}_R \\ \alpha_G\mathbf{W}_{mG}\mathbf{m}_G \end{matrix} \right\|^2 + \left\| \begin{matrix} \mathbf{m}_R - \mathbf{m}_{0R} \\ \mathbf{m}_G - \mathbf{m}_{0G} \end{matrix} \right\|^2_{\mathbf{C}_{\mathbf{RR}}^{-1}} \right\} \tag{11}$$

$$subject\ to\ t(\mathbf{m}_R, \mathbf{m}_G) = 0$$

where $\mathbf{d}_R$ is the logarithm of measured apparent resistivities, $\mathbf{d}_G$ represents the measured gravity gradient data, $\mathbf{A}_R$ and $\mathbf{A}_G$ are resistivity and gravity gradient forward operators, respectively, and $\mathbf{C}_{DD}$ is the observed data covariance matrix. $\mathbf{m} = [\mathbf{m}_R, \mathbf{m}_G]^T$ represents the model parameters, $\mathbf{m}_{0R}$ and $\mathbf{m}_{0G}$ stand for the beginning models of both techniques with covariance matrix $\mathbf{C}_{RR}^{-1}$, and $t(\mathbf{m}_R, \mathbf{m}_G)$ represents the cross-gradient values for all cells of the model. α_R and α_G are regularisation coefficients linked to the regularisation of resistivity and density matrices, $\mathbf{W}_{mR}$ and $\mathbf{W}_{mG}$, known as model weighting matrices [30]. These matrices are obtained by multiplying compactness [31] and depth weighting [32,33] functions.

Applying Lagrangian multipliers to Equation (11) results in the following system of equations, as shown by Gallardo et al. [9]:

$$\mathbf{m} = \mathbf{N}_1^{-1}\mathbf{n}_2 - \mathbf{N}_1^{-1}\mathbf{B}^T\left(\mathbf{B}\mathbf{N}_1^{-1}\mathbf{B}^T\right)^{-1}(\mathbf{B}\mathbf{N}_1^{-1}\mathbf{n}_2 - \mathbf{B}\mathbf{m}_0 + \mathbf{t}_0) \tag{12}$$

where

$$\mathbf{N}_1 = \begin{bmatrix} \mathbf{A}_R^T\mathbf{A}_R + \alpha_R^2\mathbf{W}_{mR} & 0 \\ 0 & \mathbf{A}_G^T\mathbf{A}_G + \alpha_G^2\mathbf{W}_{mG} \end{bmatrix} \tag{13}$$

and

$$\mathbf{n}_2 = \begin{bmatrix} \mathbf{A}_R^T\{\mathbf{d}_R - \mathbf{A}_R\mathbf{m}_{0R}\} \\ \mathbf{A}_G^T\{\mathbf{d}_G - \mathbf{A}_G\mathbf{m}_{0G}\} \end{bmatrix} \tag{14}$$

Matrix $\mathbf{B}$ is the Jacobian of $\mathbf{t}$, whereas $\mathbf{t}_0$ is the cross-gradient function for the initial resistivity and density models $(\mathbf{m}_{0R}, \mathbf{m}_{0G})$. The joint inversion solution (Equation (12)) has two terms. The first term represents the independent (separate) inversion of both datasets, whereas the second term describes the impact of one inverse model influencing the other via a cross-gradient constraint. The sum of these two factors leads to a combined inversion solution.

The flow diagram in Figure 5 represents the joint inversion method. The process of iterative separate and joint inversions begins concurrently, with the cross-gradient constraint ensuring that the models obtained from the resistivity inversion during each iteration constrain the models obtained from the gravity gradient inversion, and vice versa. Therefore, it is crucial to use effective separate inversion approaches by applying suitable restrictions.

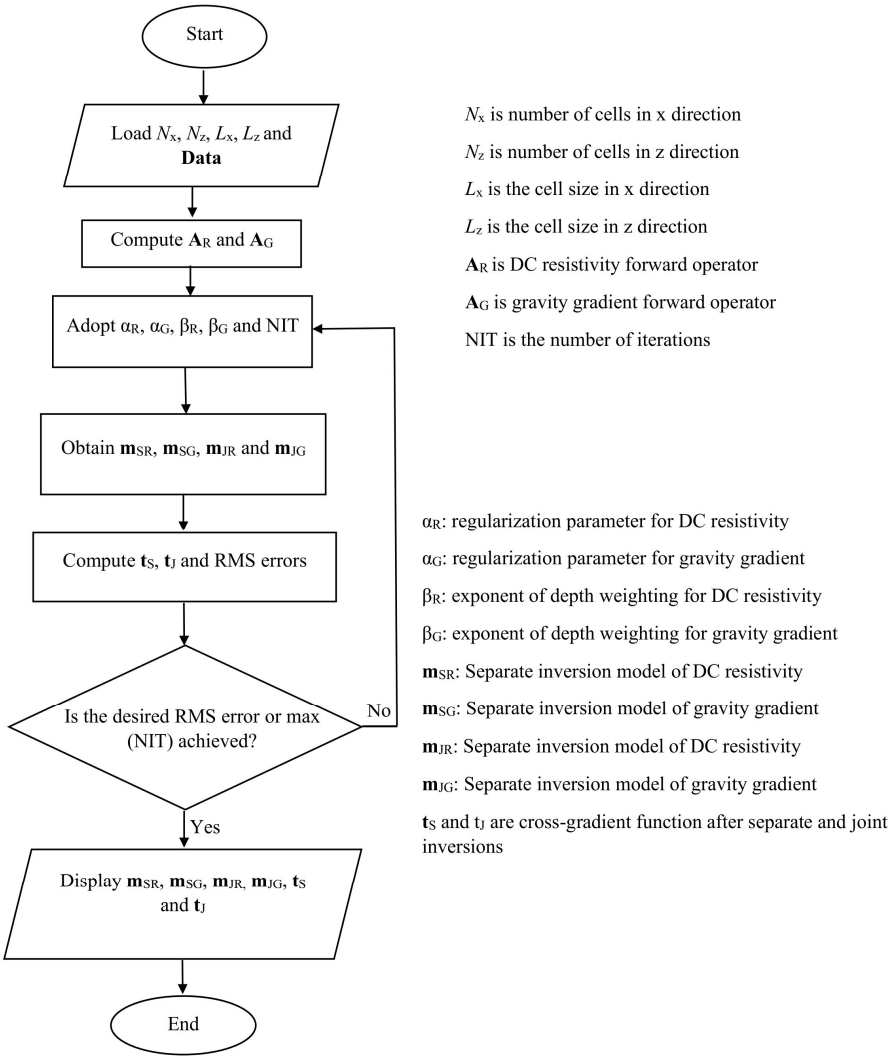

Figure 5. Flow diagram describing the joint inversion algorithm.

4. Results

4.1. Synthetic Models

4.1.1. Synthetic Model I

Adding noise to geophysical data is a common practice for simulating measurement errors and testing the robustness and stability of the algorithms. This is because errors in data collection, environmental factors, and equipment limitations often cause noise to impact measurements taken in the real world. Here, to evaluate our algorithms, data are subjected to Gaussian (normal) noise, which is usually used by researchers [34,35]. Therefore, in the following, we have added Gaussian noise with a range of 2% to the data amplitude of the two methods for both artificial models.

All parameters used in this work for the synthetic models and case studies are outlined in Table 2. In this table, α_R and α_{GG} denote the regularisation parameters for the resistivity and the gravity gradient data, respectively, which have been estimated after several trials. β_R indicates the exponent of depth weighting for resistivity, β_{GG} is the exponent of depth weighting for the gravity gradient, and NITs refer to the number of iterations. In the case of gravity fields, the depth weighting exponent is closely related to the source geometry, and its optimal choice has been a topic of discussion in several studies (e.g., [29,36]). In this study, we determine the appropriate β by analysing the behavior of the cross-gradient function and selecting the value that achieves the greatest minimisation.

Table 2. Summary of inversion parameters for all models.

Model	α_R	α_{GG}	β_R	β_{GG}	NITs
Synthetic Model I	0.5	0.01	0.7	1	5
Synthetic Model II	1.2	0.03	0.6	1	7
Case Study I	0.9	0.08	0.5	1	4
Case Study II	0.6	0.4	0.5	1	4

The joint inversion procedure for synthetic Model I started with an initial homogeneous resistivity model with a resistivity of 100 Ω-m and a background mass density of 0 g/cm^3. Figure 6a,b show the separate and joint inversion results for the DC resistivity data, respectively.

In the separate inversion result (Figure 6a), only the rightmost anomaly is reconstructed, and the central and left bodies are not well resolved. The depth extent of the leftmost body is significantly underestimated, and the boundaries of the anomalies are not well defined. This indicates the limitations of using resistivity data alone in complex subsurface scenarios.

In contrast, the joint inversion result (Figure 6b) shows a substantial improvement in the accuracy of the resistivity model. The leftmost anomaly is now more clearly resolved, especially in terms of its depth extent. The joint inversion procedure leverages the additional information provided by the gravity gradient data to enhance the overall model accuracy. The central body, however, remains partially unresolved, with a small region of low resistivity appearing beneath and to the right of it.

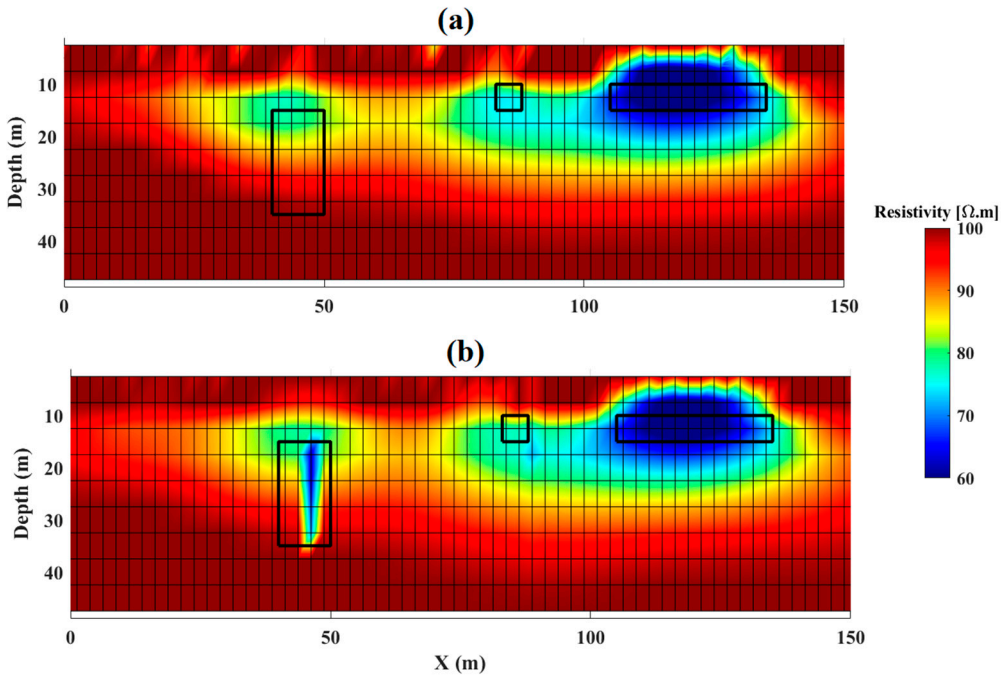

Figure 6. Inverse resistivity models for synthetic Model I after (**a**) separate and (**b**) joint inversion procedures.

The result of the gravity gradient separate inversion (Figure 7a) shows several distinct high-density regions with sharp boundaries, especially noticeable between the depths of approximately 10 to 20 m. One key feature is the fragmentation of high-density structures, on the right side of the model. The high-density anomaly appears as discrete and fragmented blocks, which could be a limitation of the separate inversion of the gravity gradient method that may not fully resolve complex structures. Also, there are potential artifacts in the inversion result, which is the effect of noise on data, visible as scattered blue zones that could be misinterpretations in regions where the signal was weak or inconsistent.

In contrast to the separate inversion, the joint inversion result (Figure 7b) shows more continuous high-density structures, especially the long anomaly on the right side of the model. This reflects the ability of joint inversion techniques to better capture complex subsurface structures by integrating different datasets. The joint inversion provides smoother and more coherent boundary definitions for the high-density anomalies. In addition, the long anomaly on the right is better resolved, suggesting that the joint inversion reduces ambiguity and provides a more reliable interpretation. Compared to the separate inversion, the joint inversion result appears cleaner, with fewer noisy or scattered low-density regions, suggesting that the joint approach has suppressed some of the artifacts present in the separate inversion.

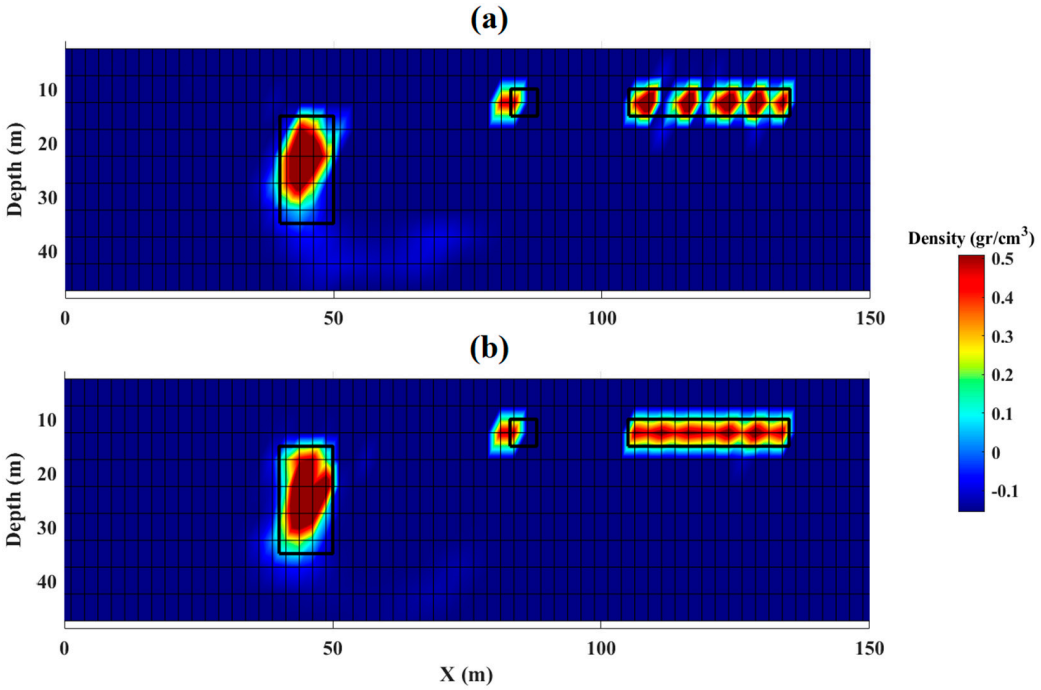

Figure 7. Inverse density models for synthetic Model I after simultaneous (**a**) separate and (**b**) joint inversion procedures.

Figure 8 displays the pseudo-sections of the observed and calculated data after separate and joint inversions for DC resistivity. Although the resistivity model obtained from the joint inversion provides a better representation of the three modelled bodies than the model obtained from the separate inversion, the RMS misfit errors of the corresponding pseudo-sections are greater for the joint inversion than for the separate inversion (2.85% vs. 3.76%). The increased error is due to the joint inversion involving an extra constraint, i.e., the cross-gradient function, which could introduce more bias and result in a greater misfit between the modelled pseudo-sections.

Figure 9 shows observed and computed gravity gradient data (g_{zz}) after the separate and combined inversions. The RMS misfit errors of the calculated data after the separate and the joint inversions for the gravity gradient approach are 4.1% and 4.8%, respectively. This similarity between the RMS errors is to be expected since near identical inverse density models were obtained from separate and joint inversions.

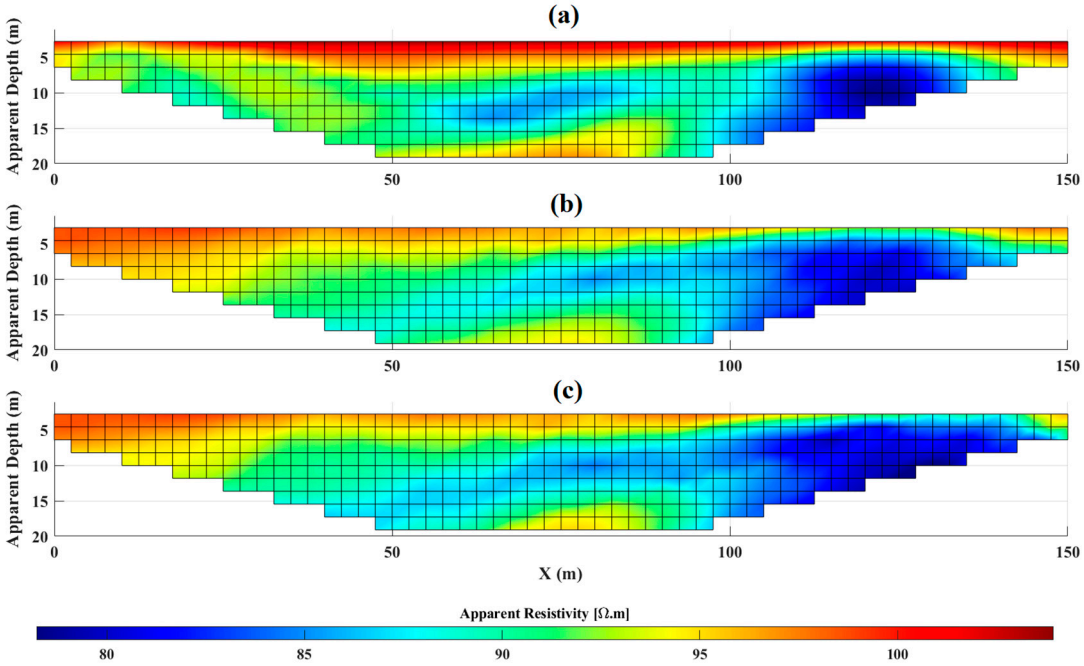

Figure 8. Pseudo-sections of synthetic Model I. (**a**) The apparent resistivity data computed from the input model, (**b**) the computed apparent resistivities corresponding to the model obtained from the separate inversion, and (**c**) the computed apparent resistivities corresponding to the model obtained from the joint inversions. The RMSE percentages for separate and joint inversions are 2.85% and 3.76%, respectively.

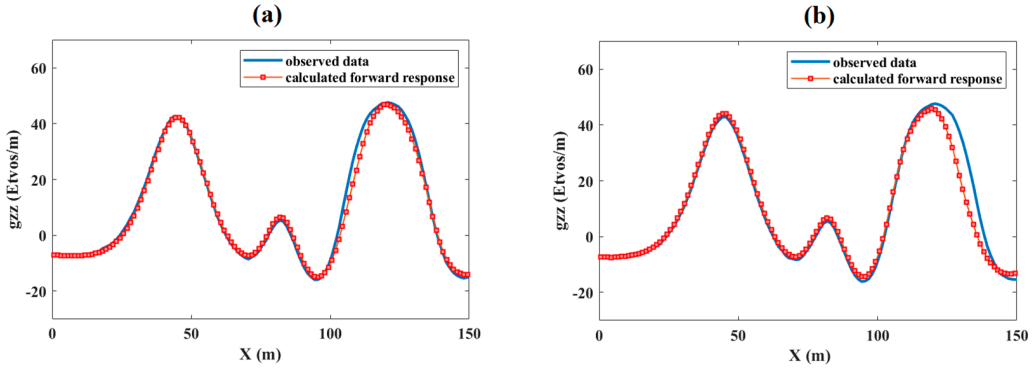

Figure 9. Forward modelled g_{zz} values for synthetic Model I. (**a**) Values computed from the input model (observed data), along with the values corresponding to the model obtained from the separate inversion, and (**b**) values computed from the input model (observed data), along with the values corresponding to the model obtained from the joint inversion. The RMSE percentages are 4.1% and 4.8% for separate and joint inversions, respectively.

Figure 10 illustrates the cross-gradient function values of the separate and the combined inverse models, showing lower values after the joint inversion. This agrees with the enhanced outcome obtained for the inverse resistivity model after the joint inversion. The increased structural similarities between the resistivity and density models after the joint inversion result in reduced values for the cross-gradient function. Indeed, the cross-gradient function is the cross-product of the gradients of the two models (Equation (8)) and enhancement of structural similarities after joint inversion means that the gradients of the resistivity and the density models are more parallel, thus leading to lower values for the cross-product of the joint inversion models.

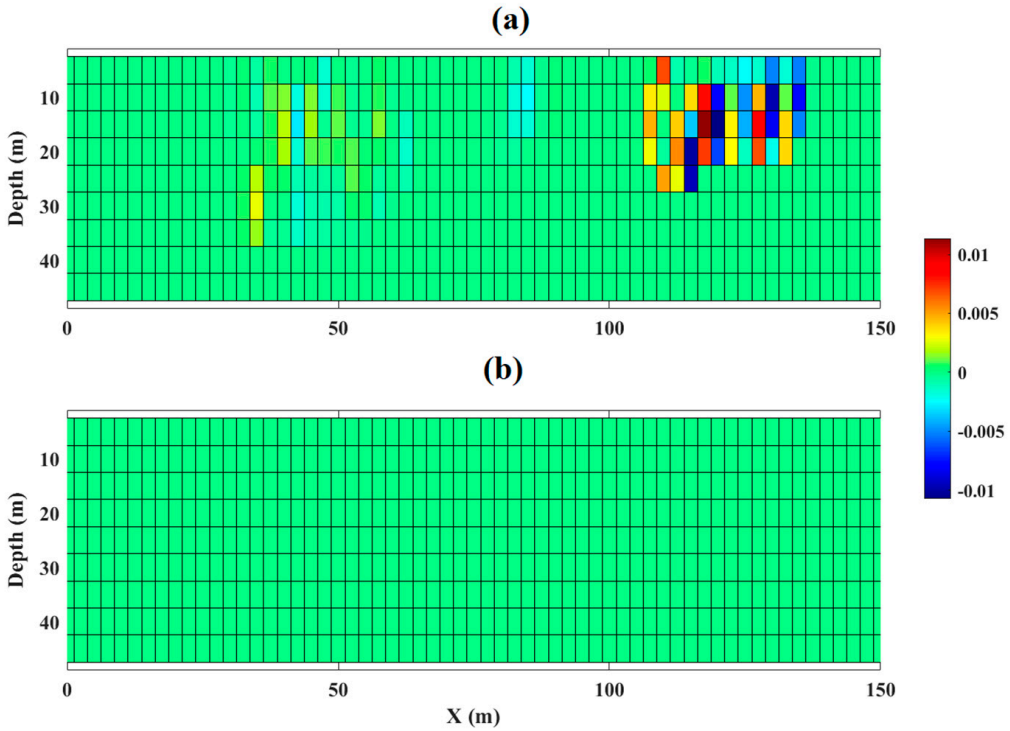

Figure 10. Cross-gradient function after (**a**) separate and (**b**) joint inversions.

4.1.2. Synthetic Model II

The calculated forward responses for synthetic Model II for both methods after adding noise (2% to the data's amplitude) are shown in Figure 11. The initial resistivity model for synthetic Model II is assumed to be uniform with a value of 300 Ωm. A regularisation parameter of 0.37 is obtained after several trials. The resistivity recovered model from the separate inversion (Figure 12a) indicates a low-resistivity anomaly (blue) centred at 150 m, extending from depths of 10 m until the bottom of the model. This denotes the simulated conductive dyke. The joint inversion yields more defined limits for the anomaly than the single inversion, especially at larger depths (Figure 12b). The low-resistivity body is clearly delineated, exhibiting more gradual transitions between the resistive and the conductive areas. The adjacent areas of elevated resistivity (red) resemble those in the individual inversion but seem to be relatively more delineated, demonstrating the benefits of joint inversion in generating a more cohesive model. The density model derived via separate inversion (Figure 12c) reveals a vertical high-density anomaly at the dyke's site.

Similar to Model I, the recovered model in this case shows, again, a sharp boundary density anomaly that is, to some extent, fragmented. This suggests that the separate inversion of the gravity gradient may have not captured the full extent of the high-density structure.

The density anomaly obtained using joint inversion reveals a more coherent and well-defined high-density structure (Figure 12d). The limits of the density anomaly are more distinct and precisely delineated, indicating that the joint inversion method is superior in defining the actual scope of the density anomaly.

In this case, the density recovered model from the joint inversion accurately resolves the thin dyke (Figure 12d), whereas the resistivity recovered model from the joint inversion (Figure 12b) gives an indication of the presence of the two layers forming the host rock and displays a zone of low resistivities around the dyke.

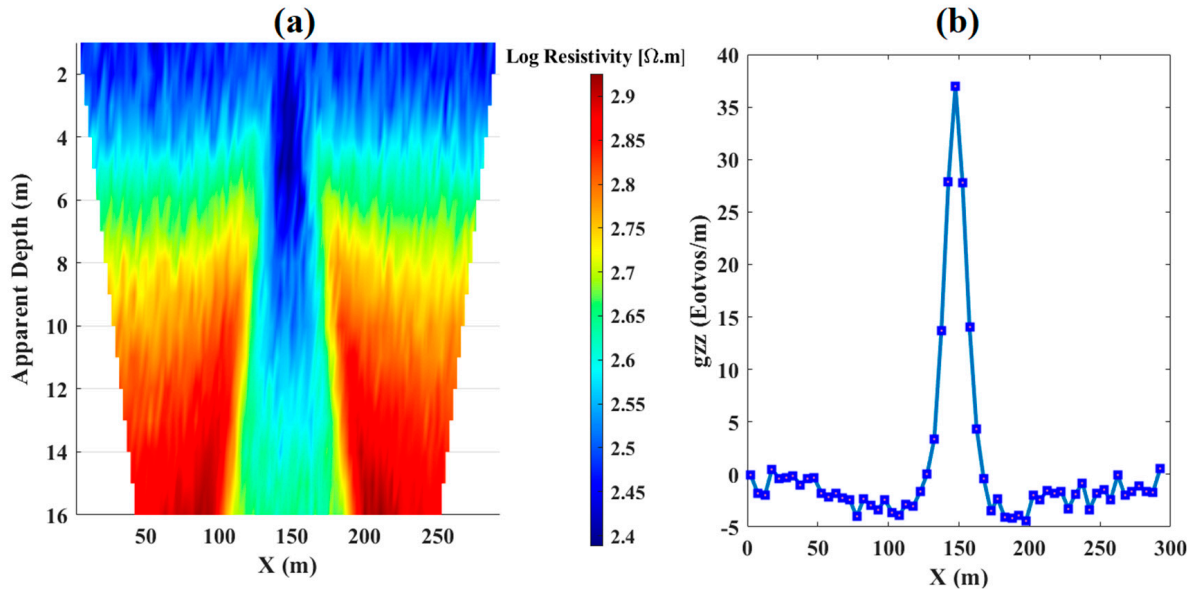

Figure 11. Contaminated forward responses of synthetic Model II with random noise. (**a**) Apparent resistivity values calculated with the Res2DMod software, and (**b**) calculated gravity gradient data.

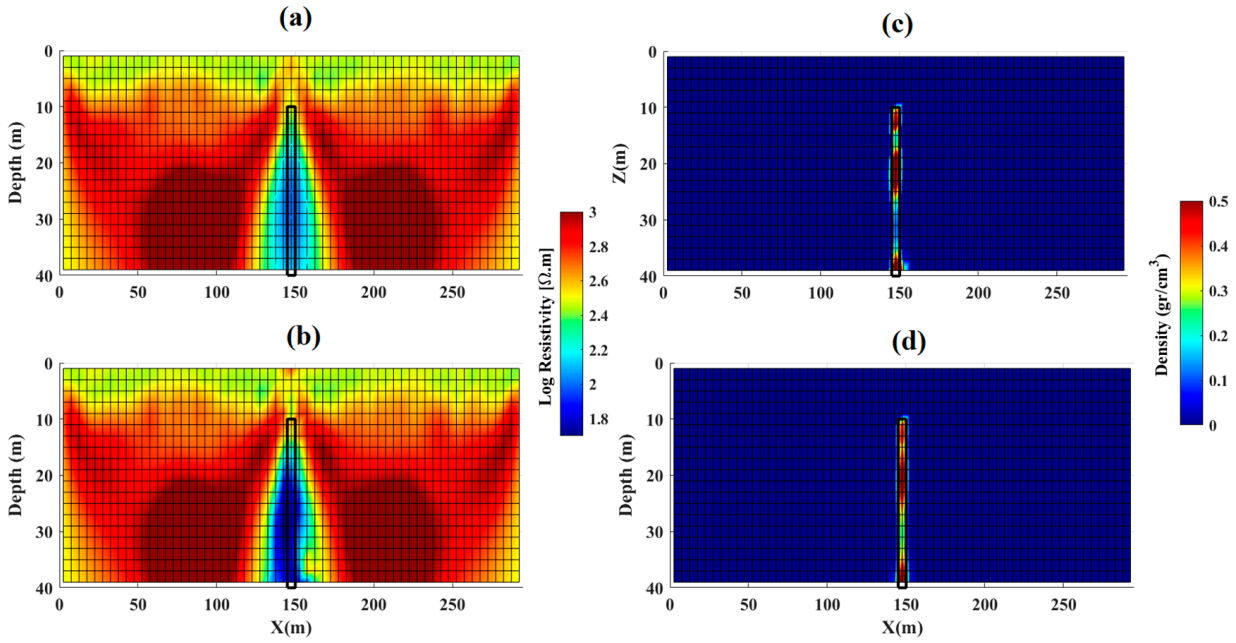

Figure 12. Inverse resistivity models after (**a**) separate and (**b**) joint inversions. Recovered density models after (**c**) separate and (**d**) joint inversions.

Figure 13 shows the resistivity pseudo-sections calculated after the separate and the joint inversions. Table 3 provides misfit errors resulting from single and combined inversions using both resistivity and gravity gradient approaches. The comparison of the misfit between the estimated forward responses and the observed data shows higher discrepancies after the joint inversion for resistivity, which is caused by the cross-gradient restriction. As discussed in the previous synthetic case, adding another restriction increases the partiality in the opposite situation, leading to a greater discrepancy in the outcome after the combined inversion. The discrepancy seen after performing separate and combined inversions for the gravity gradient approach aligns with the lack of activity in the cross-gradient function.

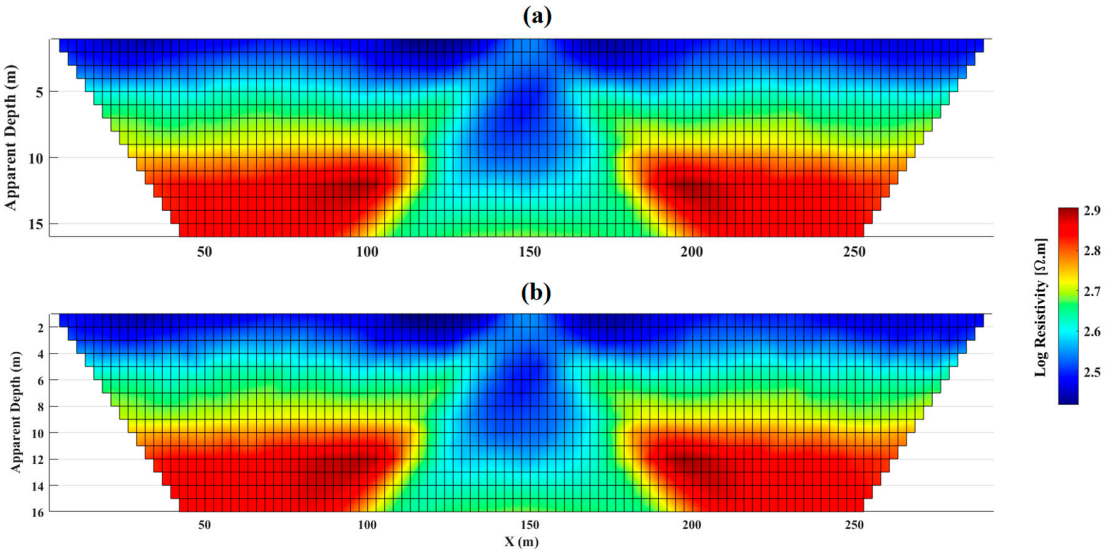

Figure 13. Pseudo-sections of computed apparent resistivities for the inverse models obtained from (**a**) separate and (**b**) joint inversions.

Table 3. Misfit errors after separate and joint inversions for resistivity and gravity gradient.

Method	After Separate Inversion	After Joint Inversion
DC Resistivity	1.86%	2.55%
Gravity Gradient	4.05%	4.18%

An effective method to evaluate the effectiveness of the cross-gradient function is by comparing the values obtained from separate and joint inversions. Due to the increase in structural similarities caused by the cross-gradient function, it is expected that the cross-gradient values from the joint inversion would be lower than those obtained from the separate inversion. The cross-gradient functions for synthetic Model II are shown in Figure 14 and clearly demonstrate this occurrence.

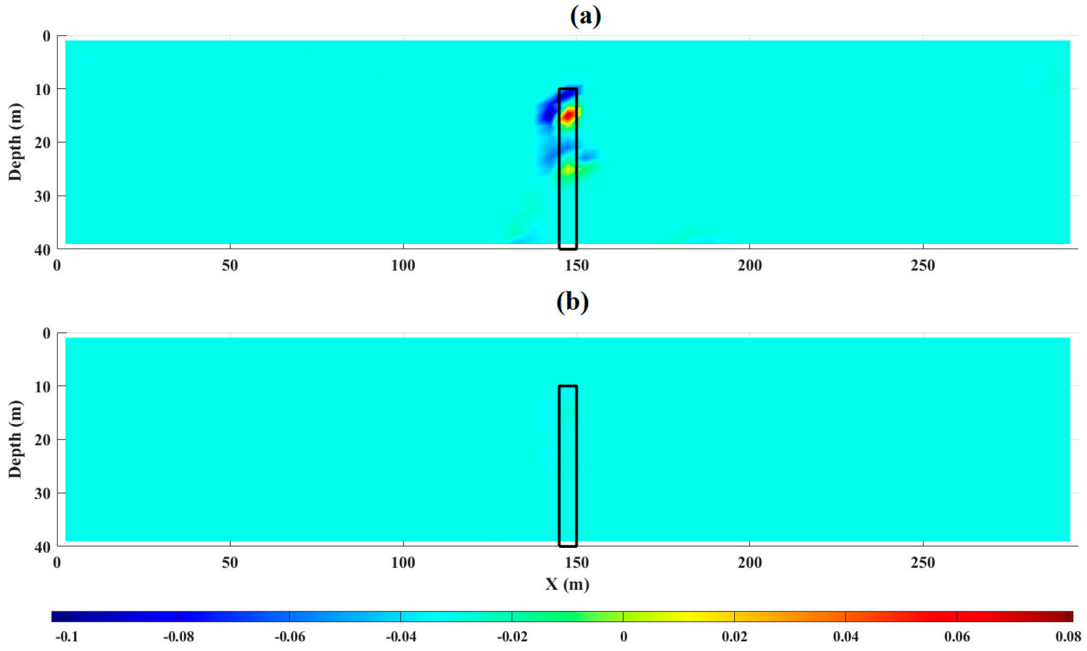

Figure 14. Cross-gradient functions after (**a**) separate and (**b**) joint inversions.

5. Case Studies

5.1. Case Study I

5.1.1. Background Information

Iran, particularly in its arid and semi-arid regions, is characterised by a scarcity of surface water sources such as lakes and rivers. In response to this environmental challenge, ancient populations developed ingenious underground water management systems known as qanats. Qanats are extensive networks of underground tunnels that were historically used to transport water from aquifers in the foothills to agricultural fields, towns, and cities across Iran. These underground water channels have played a vital role in sustaining the population and agriculture, particularly in regions where surface water is limited. The qanat system was a remarkable feat of ancient engineering, with sloping tunnels that used gravity to direct water over long distances without the need for mechanical pumps. Eleven of the qanat structures have been recently included on the UNESCO World Heritage List, emphasising their cultural, social, political, and physical significance [37]. The main reasons for the registration of qanats include their historical importance, complex system, and benefits for the ecosystem. However, as urbanisation expanded and modern infrastructure replaced traditional methods, many qanats fell into disrepair. Over time, these ancient channels have collapsed or disintegrated due to neglect, natural erosion, and urban development. As well as harming the integrity of these historical structures, this situation poses a significant risk to modern urban infrastructure and the built environment management. As the qanats collapse, they create voids beneath the surface that can lead to ground subsidence. This threatens buildings, roads, and other essential infrastructure, particularly in densely populated urban areas. Therefore, identifying the locations and conditions of these ancient water channels is crucial for the conservation of historic infrastructure systems, as well as for safeguarding the integrity of the overlying structures and preventing potentially catastrophic collapses [38]. The city of Kerman, situated in southern Iran, serves as the focal point for this case study (Figure 15). Kerman is one of the largest and most historically significant cities in the region, located in an alluvial plain characterised by fine silt and clay lithology. This alluvial plain gently slopes from the surrounding foothills towards the city, forming the foundation upon which most of the city's infrastructure has been constructed. The combination of Kerman's arid climate, historical reliance on qanats, and modern urban development makes it particularly vulnerable to the risks associated with the collapse of these underground tunnels [39].

Figure 15. Fieldwork and data collection at the study site, Kerman, Iran: geophysical measurements and qanat investigation.

The aim of this case study is to employ geophysical techniques, including electrical resistivity and gravity gradient methods, to map the subsurface structures of a region between the two residential complexes of Maskan-e-Mehr in Kerman city (Figure 15). The Maskan-e-Mehr Project, established as a national initiative by the Iranian government, aims to address the housing needs of low-income populations by providing affordable housing solutions. Figure 16 shows some of the damage to roads and the surface resulting from the collapse of qanat outlets in the investigated site. This evidence formed part of the information considered for the estimation of the qanats' position and depth. Understanding the current state of these qanats and their impact on the surrounding infrastructure will contribute valuable insights to urban planning, risk mitigation, and the preservation of this historical engineering legacy.

Figure 16. Evidence of qanat outlets collapse and related surface damage at the investigated site.

5.1.2. Geophysical Data

Three qanat outlets, called Mazhar, were clear on the surface; therefore, due to the constant slope and direct excavation of the tunnels, or gallery, in the excavation of qanats, we were able to estimate the approximate location and depth of the gallery. The tunnel, or gallery, has a slope gradient of 0.4% to maintain a balance between excessive erosion and sedimentation of the tunnel bed [40]. It should be mentioned that the purpose of the geophysical survey in this study was to confirm these calculations.

The geophysical surveys performed on a profile perpendicular to the three known qanats near Kerman consisted of a resistivity survey and a gravity gradient survey. The qanats are known to be approximately horizontal and their subsurface positions and dimensions are listed in Table 4.

Table 4. Estimated physical dimensions and subsurface positions of the investigated three qanat outlets.

Coordinates	Left Outlet	Central Outlet	Right Outlet
X (m)	23–26	43–47	54–57
Depth (m)	3–6	6–9	4–8

Figure 17 displays a simplified 3D model that reconstructs the area under investigation, showing the estimated dimensions and locations of the qanat outlets relative to the geophysical profile. The resistivity survey was conducted using the dipole–dipole configuration with a unit electrode spacing of 4 m, and values of n (AB/MN) ranging from 1 to 10. The g_{zz} data were recorded on a station spacing of 2 m and a profile length of 72 m.

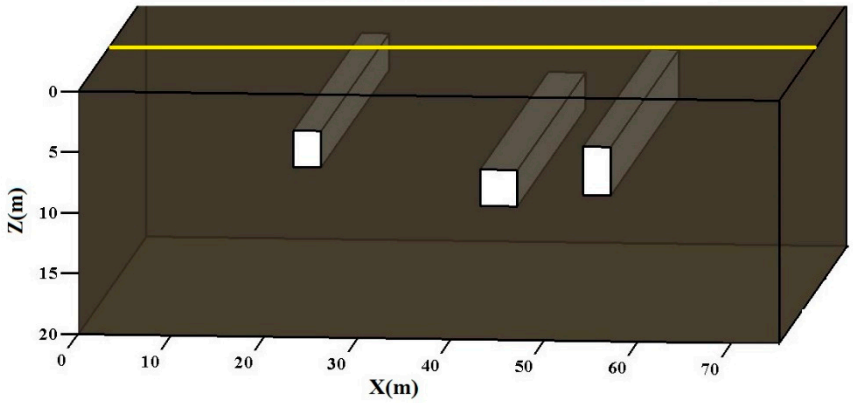

Figure 17. A three-dimensional estimated model of the area under investigation, showing the position and dimension of the qanat outlets as well as the position of the geophysical profile. The yellow line indicates the position of the collected profile.

Figure 18a displays the pseudo-section of the recorded apparent resistivity data, whereas Figure 18b shows a profile of the measured g_{zz} data.

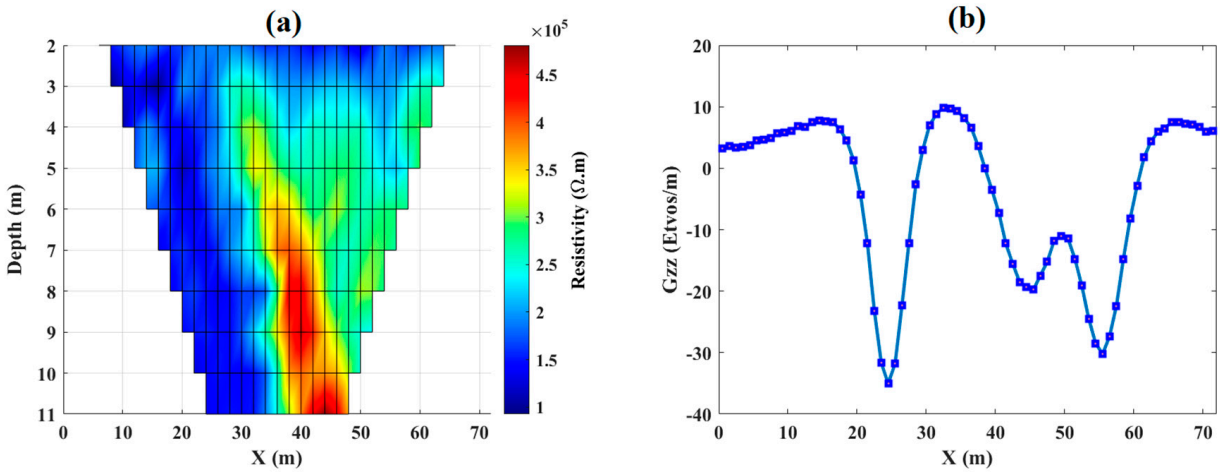

Figure 18. (**a**) Pseudo-section of the measured apparent resistivity and (**b**) profile of the gravity gradient (g_{zz}) data.

5.1.3. Results of Separate and Joint Inversions

Figure 19 shows the inverse models obtained from both separate and joint inversion. The inverse resistivity model obtained from separate inversion (Figure 19a) successfully detects the leftmost outlet qanat in its true location but fails to resolve the boundaries of the other two outlets. Furthermore, the depth extent of the deepest outlet at the centre of the profile is not retrieved effectively. In contrast, the inverse density model accurately images the three outlets, which appear as zones of low mass density in the inverse model (Figure 19c).

During the joint inversion of the two datasets, the incorporation of the g_{zz} data improves the inverse resistivity model through the cross-gradient function. In other words, the process of resistivity inversion is constrained by the density model derived from the inversion of the g_{zz} data. The inverse resistivity model obtained from the joint inversion accurately retrieves all three qanats as localised zones of high resistivity that agree well with the known positions and dimensions of the qanat outlets (Figure 19b). The inverse density model obtained from the joint inversion (Figure 19d) also exhibits some improvements over the model obtained from the separate inversion (Figure 19c). The localised zones of low density associated with the rightmost two outlets are more compact with less smearing after the joint inversion.

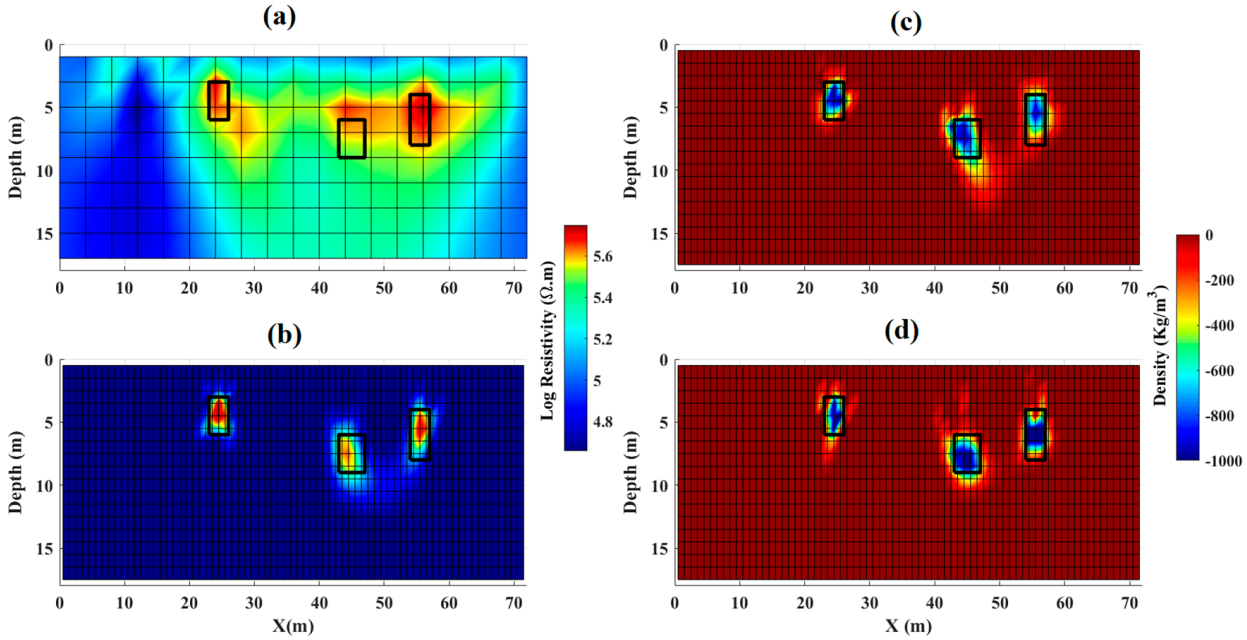

Figure 19. Inverse resistivity model after (**a**) the separate and (**b**) the joint inversions. Inverse density models after (**c**) the separate and (**d**) the joint process.

5.2. Case Study II

5.2.1. Background Information

South Africa is a nation experiencing water shortage and water-quality difficulties due to its location in a region with rising levels of water scarcity. These challenges are further exacerbated by population expansion and social and economic development concerns [41]. Groundwater serves as an alternative freshwater source for home, industrial, agricultural, and other sectors. Geophysical methods are frequently used in groundwater exploration programs to acquire insight into the subsurface conditions and reduce the risk of drilling unsuccessful supply boreholes.

Research by Woodford and Chevallier [42] in the Karoo Supergroup indicates that groundwater exploration generally focuses on dolerite dykes and sill structures. The sedimentary host rocks in contact with the intrusive formations are often significantly altered due to the high pressures and temperatures that occur during intrusion. The high fracture densities in the altered zones result in higher hydraulic conductivities relative to the host rock. These zones are generally favoured targets for groundwater exploration due to their role as suitable channels for groundwater migration [42,43]. In this context, the present study aims to map the subsurface structure of a dyke in South Africa to retrieve key information regarding the location of potential groundwater channels. Hence, understanding the subsurface layout and location of dolerite dykes through advanced geophysical methods will have a clear impact on the detection of unknown natural resources, contributing to more effective and sustainable management programs.

5.2.2. Geophysical Data

The University of the Free State recorded geophysical data across a thin dolerite dyke in sedimentary host rocks on the farm, Morgenzon, approximately 40 km northeast of the town of Bloemfontein. The geophysical methods used for this purpose were the magnetic, electromagnetic, electrical resistivity tomography (ERT), and gravity methods. More information on the geophysical surveys is provided by [43,44].

The ERT survey across the dolerite dyke was centred on the dyke and conducted with the Wenner–Schlumberger array using 81 electrodes with a standard electrode spacing of 5 m. A total of 1200 apparent resistivity measurements were taken along the profile.

The gravity survey was conducted on the same profile as the ERT survey, but gravity measurements were taken at a station spacing of 10 m, yielding 41 measurements of gravitational acceleration. Figure 20 shows the pseudo-section of the recorded apparent resistivity data and a profile of the gravity gradient data.

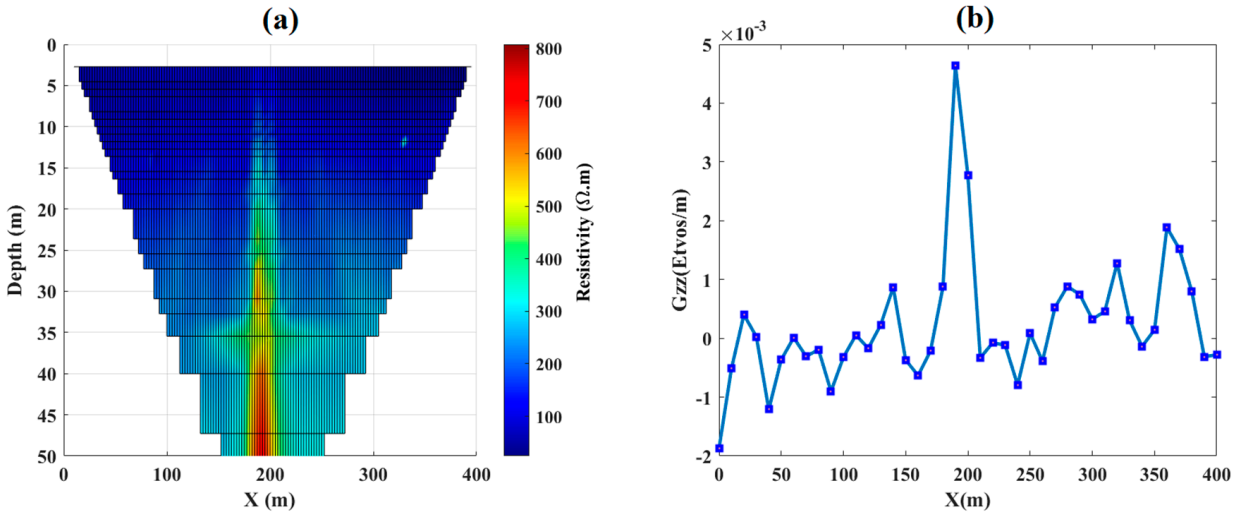

Figure 20. (**a**) Pseudo-section of the measured apparent resistivity and (**b**) profile of the gravity gradient (g_{zz}) data.

5.2.3. Results of Separate and Joint Inversions

The inverse resistivity model obtained from the separate inversion of the resistivity data alone reveals a two-layered subsurface (Figure 21a) with an irregular boundary between the two layers. Near the centre of the model where the dyke is known to occur, a resistive feature is seen that extends to the near surface, but it seems to disappear below a depth of 10 m where a zone of low resistivity is observed. At depths greater than 10 m, resistive zones are noticed on either side of this low-resistivity zone. These zones appear to fan out with increasing depth.

The separate inversion of the gravity gradient data yields the model presented in Figure 21c. The inverse density model indicates the presence of a vertical high-density structure with approximately uniform thickness near the centre of the profile, extending from a depth of 5 m to around 20 m. This high-density feature in the inverse model can be attributed to the dolerite dyke that occurs at this position.

Figure 21b and c show the results of the joint inversion conducted on the resistivity and gravity gradient data using the cross-gradient constraint, which forces the inverse models to exchange information with each other. The inverse models obtained from the joint inversion exhibit considerable improvement in the recovery of the vertical structure located in the centre of the profile. Below a depth of approximately 5 m in the inverse resistivity model, the dolerite dyke embedded in a stratified medium is clearly visible as a zone of high resistivity that extends to the bottom of the model (Figure 21b). However, this zone is again observed to fan out with depth, creating the impression that the thickness of the dykes increases with depth. The vertical structure of high density is imaged much more clearly in the inverse density model obtained from the joint inversion than in the model obtained from the separate inversion. This feature is now seen to extend to the bottom of the model, retaining its nearly uniform width along its entire depth extent (Figure 21d).

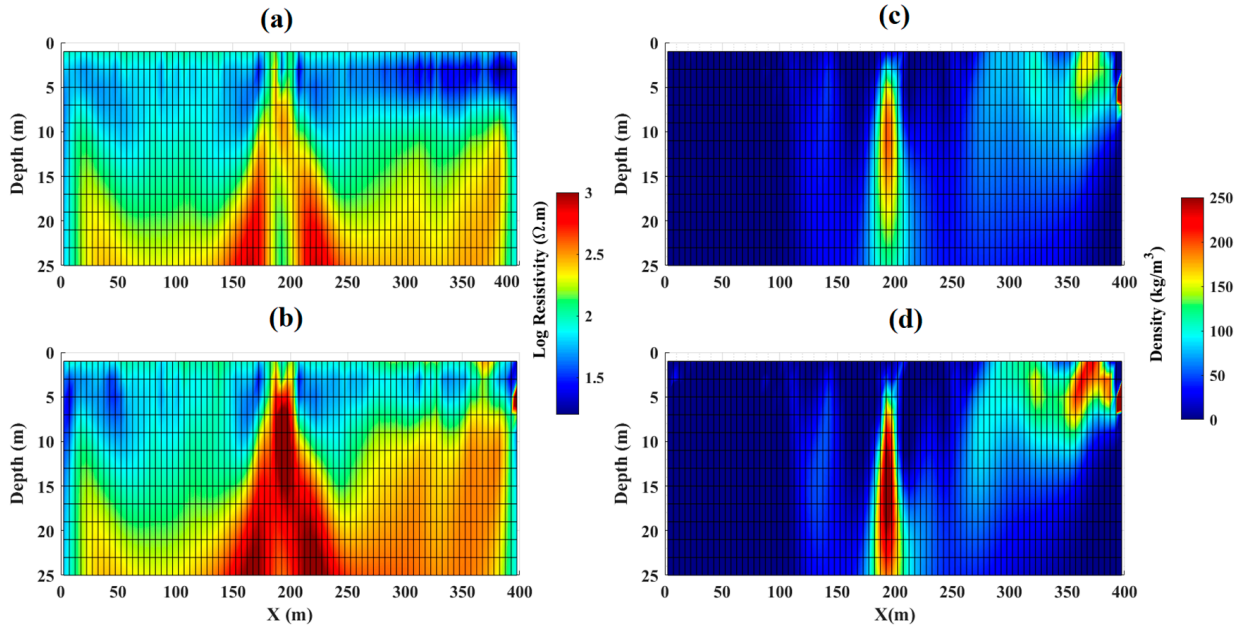

Figure 21. (**a**) Inverse resistivity model obtained from the separate inversion, (**b**) inverse resistivity model obtained from the joint inversion, (**c**) inverse density model obtained from the separate inversion, and (**d**) inverse density model obtained from the joint inversion.

6. Conclusions

This research demonstrates that joint inversion enhances the accuracy of the resistivity and the density model resolution by imposing structural similarities, as opposed to the separate inversion approaches that can yield fragmented and incoherent information on the structures. The cross-gradient constraint compels the models to interact based on common structural features, resulting in more realistic and convergent models that fulfil the requirements of both datasets. The methodology encompasses the use of synthetic and real field datasets, with the latter collected to explore the location of subsurface qanats and a dolerite dyke, in Iran and South Africa, respectively. The findings from both the synthetic and the real field datasets demonstrate the capability of joint inversion to delineate complex subsurface features. Joint inversion enhances the delineation of boundaries and promotes continuity in anomaly structures within synthetic models, which is essential for precise geological interpretation. Gravity gradient inversion is effective for ascertaining the physical and geometrical parameters of compact sources; however, it poses challenges in extracting information regarding deeper and elongated structures. When resistivity data are incorporated into a joint inversion framework, the geometry and deeper sections of the source can be more accurately constrained and reconstructed, as highlighted by the thin dyke case. However, this integration resulted in an increase in the misfit error values (Tables 2 and 3). Notably, the cross-gradient function values decreased, indicating an improvement in the consistency and quality of the reconstructed model. The cross-gradient-based joint inversion approach shows significant outcomes for improving subsurface imaging and should be considered an essential tool in geophysical research. In the practical applications investigated in this study, the use of joint inversions has enhanced the resolution of the subsurface features, providing more dependable insights for multi-disciplinary purposes. These include resource exploration, water management, cultural heritage preservation, and infrastructure risk evaluation for the built environment. Future research may further investigate this technique and assess its applicability in broader geophysical contexts.

Author Contributions: Conceptualisation, S.P. and R.V.; methodology, H.G., S.P. and R.V.; software, M.M., S.P. and R.V.; validation, H.G., M.M., F.D.F. and F.T.; formal analysis, S.P. and R.V.; investigation, H.G., M.M., F.D.F. and F.T.; resources, H.G., M.M., F.D.F. and F.T.; data curation, S.P., H.G. and R.V.; writing—original draft preparation, S.P. and R.V.; writing—review and editing, M.M., F.D.F. and F.T.; visualisation, S.P. and R.V.; supervision, F.D.F. and F.T.; project administration, F.D.F. and F.T. All authors have read and agreed to the published version of the manuscript.

Funding: This research received no external funding.

Data Availability Statement: The data and results supporting the findings of this study are available upon reasonable request from the corresponding author.

Acknowledgments: The corresponding author acknowledges the Vice-Chancellor's PhD Scholarship from the University of West London.

Conflicts of Interest: The author responsible for correspondence affirms the absence of any conflicts of interest.

References

1. Soupios, P.; Akca, I.; Mpogiatzis, P.; Basokur, A.T.; Papazachos, C. Applications of hybrid genetic algorithms in seismic tomography. *J. Appl. Geophys.* **2011**, *75*, 479–489. [CrossRef]
2. Edigbue, P.; Demirci, I.; Akca, I.; Hamdan, H.A.; Kirmizakis, P.; Soupios, P.; Candansayar, E.; Hanafy, S.; Al-Shuhail, A. A comprehensive study of local, global, and combined optimization methods on synthetic seismic refraction and direct current resistivity data. *Appl. Sci.* **2022**, *12*, 11589. [CrossRef]
3. Shi, Z.; Wang, C. Near-surface imaging by joint inversion of ERT and seismic traveltime data with guided FCM clustering. *J. Appl. Geophys.* **2024**, *222*, 105332. [CrossRef]
4. Yang, B.; Xu, K.; Liu, Z. Fuzzy constrained inversion of magnetotelluric data using guided fuzzy c-means clustering. *Surv. Geophys.* **2021**, *42*, 399–425. [CrossRef]
5. Gallardo, L.A.; Meju, M.A. Characterization of heterogeneous near-surface materials by joint 2D inversion of dc resistivity and seismic data. *Geophys. Res. Lett.* **2003**, *30*. [CrossRef]
6. Moher, D.; Liberati, J. Tetzlaff. D.G.; PRISMA GROUP, T. Preferred reporting items for systematic reviews and meta-analyses: The PRISMA statement. *Ann. Intern. Med.* **2009**, *151*, 264–269. [CrossRef] [PubMed]
7. Gallardo, L.A.; Meju, M.A. Joint two-dimensional cross-gradient imaging of magnetotelluric and seismic traveltime data for structural and lithological classification. *Geophys. J. Int.* **2007**, *169*, 1261–1272. [CrossRef]
8. Fregoso, E.; Gallardo, L.A. Cross-gradients joint 3D inversion with applications to gravity and magnetic data. *Geophysics* **2009**, *74*, L31–L42. [CrossRef]
9. Gallardo, L.A.; Meju, M.A. Joint two-dimensional DC resistivity and seismic travel time inversion with cross-gradients constraints. *J. Geophys. Res. Solid Earth* **2004**, *109*. [CrossRef]
10. Tarantola, A.; Valette, B. Inverse problems = quest for information. *J. Geophys.* **1982**, *50*, 159–170.
11. Hu, W.; Abubakar, A.; Habashy, T.M. Joint electromagnetic and seismic inversion using structural constraints. *Geophysics* **2009**, *74*, R99–R109. [CrossRef]
12. Doetsch, J.; Linde, N.; Binley, A. Structural joint inversion of time-lapse crosshole ERT and GPR traveltime data. *Geophys. Res. Lett.* **2010**, *37*. [CrossRef]
13. Bennington, N.L.; Zhang, H.; Thurber, C.H.; Bedrosian, P.A. Joint inversion of seismic and magnetotelluric data in the Parkfield Region of California using the normalized cross-gradient constraint. *Pure Appl. Geophys.* **2015**, *172*, 1033–1052. [CrossRef]
14. Joulidehsar, F.; Moradzadeh, A.; Ardejani, F.D. An improved 3D joint inversion method of potential field data using cross-gradient constraint and LSQR method. *Pure Appl. Geophys.* **2018**, *175*, 4389–4409. [CrossRef]
15. Varfinezhad, R.; Oskooi, B. 2D DC resistivity forward modeling based on the integral equation method and a comparison with the RES2DMOD results. *J. Earth Space Phys.* **2020**, *45*, 43.
16. Bianco, L.; Tavakoli, M.; Vitale, A.; Fedi, M. Multi-Order Sequential Joint Inversion of gravity data with inhomogeneous depth weighting: From near surface to basin modelling applications. *IEEE Trans. Geosci. Remote Sens.* **2023**, *62*, 1–11. [CrossRef]
17. Gallardo, L.A.; Meju, M.A. Structure-coupled multiphysics imaging in geophysical sciences. *Rev. Geophys.* **2011**, *49*. [CrossRef]
18. Zhou, J.; Xiu, C.; Zhang, X. Simultaneous structure-coupled joint inversion of gravity and magnetic data based on a damped least-squares technique. *Int. J. Geosci.* **2015**, *6*, 172–179. [CrossRef]
19. Meju, M.A.; Gallardo, L.A. Structural coupling approaches in integrated geophysical imaging. *Integr. Imaging Earth Theory Appl.* **2016**, 49–67. [CrossRef]
20. Wang, K.-P.; Tan, H.-D.; Wang, T. 2D joint inversion of CSAMT and magnetic data based on cross-gradient theory. *Appl. Geophys.* **2017**, *14*, 279–290. [CrossRef]
21. Zhang, R.; Li, T. Joint inversion of 2D gravity gradiometry and magnetotelluric data in mineral exploration. *Minerals* **2019**, *9*, 541. [CrossRef]
22. Blakely, R.J. *Potential Theory in Gravity and Magnetic Applications*; Cambridge University Press: Cambridge, UK, 1996.

23. Varfinezhad, R.; Fedi, M.; Milano, M. The role of model weighting functions in the gravity and DC resistivity inversion. *IEEE Trans. Geosci. Remote Sens.* **2022**, *60*, 1–15. [CrossRef]
24. Varfinezhad, R.; Parnow, S.; Florio, G.; Fedi, M.; Vizheh, M.M. DC resistivity inversion constrained by magnetic method through sequential inversion. *Acta Geophys.* **2023**, *71*, 247–260. [CrossRef]
25. Parnow, S.; Oskooi, B.; Florio, G. Improved linear inversion of low induction number electromagnetic data. *Geophys. J. Int.* **2021**, *224*, 1505–1522. [CrossRef]
26. Zhdanov, M.S. *Geophysical Electromagnetic Theory and Methods*; Elsevier: Amsterdam, The Netherlands, 2009.
27. Pérez-Flores, M.; Méndez-Delgado, S.; Gómez-Treviño, E. Imaging low-frequency and dc electromagnetic fields using a simple linear approximation. *Geophysics* **2001**, *66*, 1067–1081. [CrossRef]
28. Charré-Meza, A.S.; Pérez-Flores, M.A.; Gómez-Treviño, E. 2-D inversion of DC resistivity data from the Cerro Prieto geothermal area, Mexico. *Proc. World Geotherm. Congr.* **2000**, *2000*, 1037–1041.
29. Cella, F.; Fedi, M. Inversion of potential field data using the structural index as weighting function rate decay. *Geophys. Prospect.* **2012**, *60*, 313–336. [CrossRef]
30. Varfinezhad, R.; Oskooi, B.; Fedi, M. Joint inversion of DC resistivity and magnetic data, constrained by cross gradients, compactness and depth weighting. *Pure Appl. Geophys.* **2020**, *177*, 4325–4343. [CrossRef]
31. Last, B.; Kubik, K. Compact gravity inversion. *Geophysics* **1983**, *48*, 713–721. [CrossRef]
32. Li, Y.; Oldenburg, D.W. 3-D inversion of gravity data. *Geophysics* **1998**, *63*, 109–119. [CrossRef]
33. Li, Y.; Oldenburg, D.W. 3-D inversion of magnetic data. *Geophysics* **1996**, *61*, 394–408. [CrossRef]
34. Zhou, J.; Revil, A.; Karaoulis, M.; Hale, D.; Doetsch, J.; Cuttler, S. Image-guided inversion of electrical resistivity data. *Geophys. J. Int.* **2014**, *197*, 292–309. [CrossRef]
35. Krahenbuhl, R.A.; Li, Y. Inversion of gravity data using a binary formulation. *Geophys. J. Int.* **2006**, *167*, 543–556. [CrossRef]
36. Vitale, A.; Fedi, M. Self-constrained potential fields through a 3D depth weighting. *Geophysics* **2020**, *85*, G143–G156. [CrossRef]
37. Mousazadeh, H.; Ghorbani, A.; Azadi, H.; Almani, F.A.; Zangiabadi, A.; Zhu, K.; Dávid, L.D. Developing sustainable behaviors for underground heritage tourism management: The case of Persian Qanats, a UNESCO world heritage property. *Land* **2023**, *12*, 808. [CrossRef]
38. Rayhani, M.H.; El Naggar, M.H. Collapse hazard zonation of qanats in greater Tehran area. *Geotech. Geol. Eng.* **2007**, *25*, 327–338. [CrossRef]
39. Aghamolaie, I.; Lashkaripour, G.; Ghafoori, M.; Hafezi Moghadas, N. Investigating the Development of Kerman's Soil Structure and its Effect on the Collapsibility index. *Int. J. Min. Geo-Eng.* **2018**, *52*, 43–51.
40. Ahmadi, H.; Nazari Samani, A.; Malekian, A. The qanat: A living history in Iran. In *Water and Sustainability in Arid Regions*; Springer: Dordrecht, The Netherlands, 2010; pp. 125–138.
41. Dennis, I.; Dennis, R. Climate change vulnerability index for South African aquifers. *Water SA* **2012**, *38*, 417–426. [CrossRef]
42. Woodford, A.; Chevallier, L. Hydrogeology of the Main Karoo Basin: Current knowledge and future research needs. *Water Res. Comm. Rep. No. TT* **2002**, *179*, 482.
43. Makhokha, D. A Systematic Approach to the Interpretation of Conductivity Anomalies Across Intrusive Dolerite Dykes and Sills in the Karoo Supergroup. Master's Thesis, University of the Free State, Bloemfontein, South Africa, 2016.
44. Makhokha, D.; Fourie, F. A systematic approach to the interpretation of conductivity anomalies across intrusive dolerite dykes and sills in the Karoo Supergroup. In Proceedings of the 14th Biennial Ground Water Division Conference and Exhibition, Muldersdrift, South Africa, 21–23 September 2015.